

## Stability of stratified flows through neo-Hookean soft-gel-coated walls

B. Dinesh, and S. Pushpavanam

Citation: *Physics of Fluids* **30**, 104103 (2018); doi: 10.1063/1.5045658

View online: <https://doi.org/10.1063/1.5045658>

View Table of Contents: <http://aip.scitation.org/toc/phf/30/10>

Published by the *American Institute of Physics*

---

### Articles you may be interested in

[The cavitating Taylor-Couette flow](#)

*Physics of Fluids* **30**, 104101 (2018); 10.1063/1.5049743

[Stable and unstable miscible displacement of a shear-thinning fluid at low Reynolds number](#)

*Physics of Fluids* **30**, 103101 (2018); 10.1063/1.5049829

[Direct numerical simulation of a turbulent Couette-Poiseuille flow with a rod-roughened wall](#)

*Physics of Fluids* **30**, 105101 (2018); 10.1063/1.5049173

[Higher-order moments with turbulent length-scales and anisotropy associated with flow over dune shapes in tidal environment](#)

*Physics of Fluids* **30**, 106602 (2018); 10.1063/1.5038433

[A one-dimensional model for compressible fluid flows through deformable microchannels](#)

*Physics of Fluids* **30**, 092003 (2018); 10.1063/1.5043202

[Dynamics of elliptic particle sedimentation with thermal convection](#)

*Physics of Fluids* **30**, 103301 (2018); 10.1063/1.5051817

---

PHYSICS TODAY

WHITEPAPERS

#### ADVANCED LIGHT CURE ADHESIVES

Take a closer look at what these environmentally friendly adhesive systems can do

READ NOW

PRESENTED BY  
 **MASTERBOND**  
ADHESIVES | SEALANTS | COATINGS

# Stability of stratified flows through neo-Hookean soft-gel-coated walls

B. Dinesh and S. Pushpavanam<sup>a)</sup>

Department of Chemical Engineering, Indian Institute of Technology Madras, Chennai 600 036, India

(Received 22 June 2018; accepted 24 September 2018; published online 11 October 2018)

The linear stability of two-phase stratified flows through soft-gel-coated walls is studied in this work. A consistent nonlinear neo-Hookean model describes the soft-gel. The base state is characterised by a first normal stress difference in this model. This results in a significantly different effect on the stability of two-phase flows as compared to when a linear viscoelastic model is used for the soft-gel. Both fluids are assumed Newtonian and incompressible. We analyze the system in the absence and presence of a soluble surfactant. A linear stability analysis is carried out to identify different instability modes in the system. The linearised equations result in a generalised eigenvalue problem which is numerically solved employing a Chebyshev collocation technique. Three distinct instabilities are identified in the absence of a soluble surfactant. A *long wave interfacial instability*, a *Tollmien-Schlichting wave type instability*, and a *gel-liquid instability* arise in the system. Two distinct additional instabilities are identified in the presence of soluble surfactants in the system, a *Marangoni driven long wave instability* and a *liquid-liquid short wave mode*. It is shown that all instabilities except the Tollmien-Schlichting shear instability can be *stabilised* by the soft-gel layers for a suitable choice of parameters. Insights into the physical mechanism driving the different instabilities are discussed. *Published by AIP Publishing.* <https://doi.org/10.1063/1.5045658>

## I. INTRODUCTION

Two-phase flows past soft-gel-coated walls at low Reynolds numbers are important in several microfluidic applications<sup>1</sup> where the micro-channels are made of soft materials like PFA (perfluoroalkoxy),<sup>2–4</sup> FEP (fluorinated ethylene-propylene), and PDMS. It is also relevant in pulmonary fluid mechanics.<sup>5,6</sup> Experimental studies have established that two-phase flows here can become unstable at much lower Reynolds numbers as compared to flows through rigid walls.<sup>7–11</sup> The elastohydrodynamic coupling between the fluids and the soft-gels plays a crucial role in determining the stability of the flow. Understanding the physics behind these flows is necessary to arrive at optimal designs of lab-on-chip devices.

Earlier studies have used a linear viscoelastic model to describe the soft-gel. This is valid only for small deformations in the soft-gel.<sup>12–17</sup> A neo-Hookean solid model on the other hand can capture large deformations in soft-gels.<sup>18</sup> Couette flows over a neo-Hookean soft-gel are characterised by a first normal stress difference in the base displacement field. Consequently the effect on stability can be significantly different from that predicted by a linear viscoelastic model. In the creeping flow limit, predictions from both the models agree qualitatively when the ratio of gel to fluid thickness is greater than unity.

Instabilities in gravity driven free-surface flows past a deformable elastic solid were studied in Ref. 19. A neo-Hookean solid model was considered to represent the elastic solid. The instability is induced by the deformable solid-fluid interface. The effect of finite Reynolds numbers on the stability

of gravity driven free surface flows past a deformable neo-Hookean solid was analyzed in Ref. 20. The free surface instability which arises at the liquid-air interface was suppressed by the deformable nature of the soft-gels. The stability of Couette flow of a Newtonian fluid past an incompressible neo-Hookean solid in the creeping flow limit was analyzed in Ref. 21. The predictions of both linear viscoelastic and neo-Hookean models yielded results which are consistent with those in Ref. 18. The neo-Hookean solid model presented in Ref. 18 did not predict any instability of a Hagen-Poiseuille flow.<sup>22</sup> A linear viscoelastic model however predicted an instability for these flows.

The stability of pressure driven creeping flows through soft channels has been recently analyzed.<sup>23</sup> Here the first normal stress difference in the base state at the soft-gel results in a short wave (SW) instability. This was absent when consistent boundary conditions were imposed at the gel-liquid (GL) interface.<sup>24</sup> A consistent Eulerian and Lagrangian formulation for flows through neo-Hookean soft-gel lined tubes and channels was presented in Ref. 25 to resolve discrepancies reported in the literature. The results obtained from both the formulations for Couette flow and Hagen-Poiseuille flows through soft walls were consistent. Manipulation of free surface instability by deformable solid bilayers was studied in Ref. 26. The effective shear modulus of the bilayer determines the free-surface stability.

Several experimental studies have analyzed different instabilities that evolve in flows over a deformable soft-gel. These were studied in the limit of low Reynolds numbers in Ref. 7. The transition from laminar flow arising from an instability for soft walls was observed for much lower Reynolds numbers compared to that in flow past rigid solids. A flow induced instability in a tube with flexible walls was studied

<sup>a)</sup> Author to whom correspondence should be addressed: spush@iitm.ac.in. Telephone: +91-44-22574161. Fax: +91-44-22570509.

experimentally.<sup>8</sup> Tubes of diameters varying from 0.8 to 1.2 mm were made using PDMS. The shear modulus of the elastic tubes varied from 17 to 550 kPa. It was found out that the laminar flow becomes unstable for Reynolds numbers as low as 500. Fluid structure interactions in deformable micro-channels were studied in Ref. 27. Experimental predictions of thin layer deformations and pressure drop were found to be in qualitative agreement with predictions of two- and three-dimensional models. The quantitative agreement of experimental and theoretical predictions for Couette flow through a two-layer neo-Hookean gel was studied in Ref. 11. An experimental and theoretical analysis of Poiseuille flow through tubes lined with neo-Hookean soft-gels was presented in Ref. 9. The Reynolds number obtained theoretically for the flow transition matched with that found experimentally, when the deformations at the base state in the soft-gels were considered after a pressure gradient was applied across the pipe. An experimental analysis of the onset of instability of Hagen-Poiseuille flow in a pipe lined with neo-Hookean soft-gels was carried out in Ref. 28. The transition Reynolds number obtained from the experiments however did not agree with the theoretical predictions.

From the above analysis of the literature, it is clear that two-phase stratified flows through soft walls are not well understood. Besides, there are several contradictory reports in the literature on the stability of these flows. In this work, we focus on using a consistent Eulerian formulation of a neo-Hookean model to represent the soft-gel.<sup>25</sup> This formulation gives insights into the effects of soft-gel layers on different two-phase flow instabilities. The model helps highlight the role of the first normal stress in the base state displacement field of the soft-gels on stability.

The paper is structured as follows. The governing equations are presented in Sec. II. The base state velocity and concentration profiles are presented in Sec. III. The linear stability analysis and the linearised governing equations are discussed in Sec. IV. The relevant boundary conditions at the liquid-liquid interface both in the absence and presence of soluble surfactants are discussed in the Appendix. A detailed energy budget analysis is presented in the supplementary material. Section V discusses the important results. First, the scaling obtained from the linear stability theory is validated with experiments for single phase flows in the literature. Then the different instabilities that arise in the absence and presence of soluble surfactants for two-phase flows are discussed. A summary of key conclusions obtained from the results is given in Sec. VI.

## II. GOVERNING EQUATIONS

We consider two-phase pressure driven stratified flows through soft-gel-coated parallel plates, as shown in Fig. 1. The fluids are assumed to be incompressible and Newtonian. The soft-gel layers are represented by a neo-Hookean model. The dimensionless continuity and Navier-Stokes equations which govern the flow of the two phases are

$$\partial_x u_j + \partial_y v_j = 0, \quad (1)$$

$$\frac{\text{Re}_1}{\mu_{j1}} \left( \partial_t u_j + u_j \partial_x u_j + \partial_y u_j v_j \right) = -\partial_x p_j + \nabla^2 u_j, \quad (2)$$

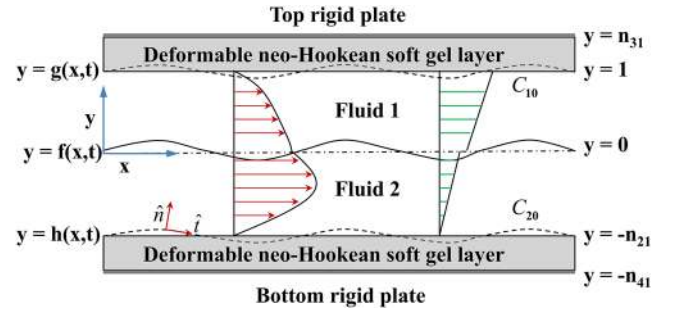


FIG. 1. Schematic of the flow configuration in the presence of soluble surfactants. Two fluids “Fluids 1” and “Fluids 2” flow side by side. The base state parabolic velocity profile is indicated by the red arrows. The perturbed liquid-liquid interface is given by  $y = f(x, t)$ . The perturbed top and bottom gel-liquid interface is given by  $y = 1 + g(x, t)$ ,  $y = -n_{21} + h(x, t)$ , respectively.  $\hat{n}$  and  $\hat{t}$  represent the normal and tangent to the perturbed bottom gel-liquid interface. The top and bottom gel-liquid interfaces are maintained at a constant solute concentration  $C_{10}$  and  $C_{20}$ . The base state concentration profile is linear and is also shown.

$$\frac{\text{Re}_1}{\mu_{j1}} \left( \partial_t v_j + u_j \partial_x v_j + v_j \partial_y v_j \right) = -\partial_y p_j + \nabla^2 v_j, \quad (3)$$

where  $j = 1, 2$  refer to the top and bottom fluids,  $\partial_t$  is  $\frac{\partial}{\partial t}$ , and  $\partial_x, \partial_y$  are similarly defined. The Laplacian is defined as  $\nabla^2 = \partial_x^2 + \partial_y^2$ . Two dimensional perturbations are introduced in the flow direction ( $x$ ) and the transverse direction ( $y$ ), and their evolution is analyzed. The flow fields are assumed independent of the  $z$ -coordinate, as the system extends to infinity in that direction. Here the Reynolds number is defined as  $\text{Re}_1 = \frac{\rho_1 U_0 d_1}{\mu_1}$ , where  $d_1, \rho_1$ , and  $\mu_1$  are the thickness, density, and viscosity of “Fluid 1.”  $U_0$  is the interfacial velocity at the liquid-liquid interface. All the dimensionless variables are defined in Table I.

The solute transport in the fluids is captured using the dimensionless species balance equation

$$\partial_t c_j + u_j \partial_x c_j + v_j \partial_y c_j = \frac{D_{j1}}{Pe} \nabla^2 c_j \quad \text{for } j = 1, 2. \quad (4)$$

$D_{j1} = \frac{D_j}{D_1}$  represents the ratio of molecular diffusivity of the solute in the “ $j$ -th fluid” to that in “Fluid 1” and  $Pe = \frac{U_0 d_1}{D_1}$  represents the Peclet number. The surface tension at the liquid-liquid interface is assumed to be linearly dependent on the concentration of the solute at the liquid-liquid interface,

$$\sigma = \sigma_0 (1 - \beta C_{10} (c_1 - c_r)). \quad (5)$$

Here  $\sigma_0$  is the surface tension at the liquid-liquid interface when the solute concentration is equal to the reference value  $C_{10} c_r$  and  $\beta = -(d\sigma/dc_1)/\sigma_0 C_{10}$ . This variation of surface tension with concentration leads to Marangoni stresses, in the tangential stress balance. This condition is given by

$$\frac{1}{(1 + (\partial_x f)^2)^{1/2}} \left[ 2 \partial_x f \mu_{j1} (v_{j,y} - u_{j,x}) + (1 - (\partial_x f)^2) \mu_{j1} (\partial_y u_j + \partial_x v_j) \right]_{j=1}^{j=2} - \frac{Ma}{Pe} (\partial_x c_1 + \partial_x f \partial_y c_1) = 0, \quad (6)$$

where  $Ma = \frac{\sigma_0 \beta C_{10} d_1}{D_1 \mu_1}$  is the modified Marangoni number and  $y = f(x, t)$  represents the perturbed liquid-liquid interface.

TABLE I. Definitions for the dimensionless parameters.

Definition	Dimensionless parameter
$n_{21} = \frac{d_2}{d_1}, n_{31} = \frac{d_3}{d_1}, n_{41} = \frac{d_4}{d_1}$	The thickness ratio of Fluid 2, top gel, and bottom gel with respect to "Fluid 1"
$\rho_{21} = \frac{\rho_2}{\rho_1}$	Ratio of density of "Fluid 2" to "Fluid 1"
$\mu_{21} = \frac{\mu_2}{\mu_1}, \mu_{31} = \frac{\mu_3}{\mu_1}, \mu_{41} = \frac{\mu_4}{\mu_1}$	Viscosity ratio of "Fluid 2," top gel, and bottom gel to "Fluid 1"
$Ca_{21} = \frac{\mu_1 U_{10}}{\sigma_{21}}, Ca_{31} = \frac{\mu_1 U_{10}}{\sigma_{31}}, Ca_{41} = \frac{\mu_1 U_{10}}{\sigma_{41}}$	Capillary number corresponding to the liquid-liquid ( $Ca_{21}$ ), top ( $Ca_{31}$ ), and bottom gel-liquid ( $Ca_{41}$ ) interfaces
$Wi_3 = \frac{\mu_3 U_0}{G_3 d_1}, Wi_4 = \frac{\mu_4 U_0}{G_4 d_1}$	Weissenberg number corresponding to the top ( $Wi_3$ ) and bottom soft-gel layers ( $Wi_4$ )
$Re_1 = \frac{\rho_1 U_0 d_1}{\mu_1}$	Reynolds number corresponding to "Fluid 1"
$Pe = \frac{U_0 d_1}{D_1}$	Peclet number
$\gamma = \frac{C_{20}}{C_{10}}$	Concentration of the soluble surfactant at the bottom gel-liquid interface to the top gel-liquid interface
$K$	Distribution coefficient
$Ma = \frac{\sigma_0 \beta C_{10} d_1}{D_1 \mu_1}$	Modified Marangoni number

We adopt the Eulerian formulation outlined in Refs. 25 and 29 to represent the neo-Hookean soft-gel-coatings. The position of a particle in the deformed ( $x_j$ ) and undeformed ( $X_j$ ) configurations is related by

$$x_j = X_j + u_{g,j}(x). \quad (7)$$

Here  $j = 3, 4$  represent the top and bottom neo-Hookean soft-gel layers. The deformation gradient tensor in this formulation is given by

$$f_j = \frac{\partial X_j}{\partial x_j} \quad \text{for } j = 3, 4. \quad (8)$$

The incompressibility condition for a neo-Hookean layer is

$$\det(f_j) = 1 \quad \text{for } j = 3, 4. \quad (9)$$

The Cauchy stress tensor for the neo-Hookean material is given by

$$\tau_j = -p_{g,j} I + G_j (f_j^T \cdot f_j)^{-1} + \mu_{g,j} (L_j + L_j^T) \quad \text{for } j = 3, 4, \quad (10)$$

where  $L_j = (\dot{f}_j^{-1} \cdot f_j)$ ,  $G_j$  is the shear modulus, and  $\mu_{g,j}$  is the viscosity of the soft-gel layers. We use this to obtain the momentum balance equations for the soft-gel layers,

$$\nabla_x \cdot \tau_j = 0 \quad \text{for } j = 3, 4. \quad (11)$$

The relation between the velocity in the solid  $V_j^g$  and the displacement field  $u_{g,j}$  is given by

$$V_j^g = \frac{\partial u_{g,j}}{\partial t} + V_j^g \cdot \frac{\partial u_{g,j}}{\partial x} \quad \text{for } j = 3, 4. \quad (12)$$

The boundary conditions continuity of velocity, continuity of tangential stresses and normal stresses are applied at the two gel-liquid interfaces.

### III. BASE STATE

The base state velocity profile in the fluids is parabolic. This is non-dimensionalized by the interfacial velocity  $U_0$ .<sup>15,30</sup> The resultant dimensionless profiles are given by

$$U_1 = 1 + a_1 y + b_1 y^2, \quad (13)$$

$$U_2 = 1 + a_2 y + b_2 y^2, \quad (14)$$

where

$$a_1 = \frac{\mu_{21} - n_{21}^2}{n_{21}^2 + n_{21}}, \quad b_1 = -\frac{\mu_{21} + n_{21}}{n_{21}^2 + n_{21}}, \quad (15)$$

$$a_2 = \frac{a_1}{\mu_{21}}, \quad b_2 = \frac{b_1}{\mu_{21}}. \quad (16)$$

The base state concentration profiles are linear in each fluid and are nondimensionalized using  $C_{10}$ ,

$$C_j = s_j y + t_j, \quad (17)$$

$$s_1 = \frac{D_{21}(1 - \gamma K)}{D_{21} + K n_{21}}, \quad t_1 = \frac{K(n_{21} + D_{21} \gamma)}{D_{21} + K n_{21}}, \quad (18)$$

$$s_2 = \frac{s_1}{D_{21}}, \quad t_2 = \frac{t_1}{K}. \quad (19)$$

The concentration profile is a function of diffusivity ratio ( $D_{21}$ ), thickness ratio ( $n_{21}$ ), distribution coefficient ( $K$ ), and concentration ratio ( $\gamma = \frac{C_{20}}{C_{10}}$ ). The direction of mass transfer is dictated by  $\gamma$ .  $\gamma < 1/K$  ( $\gamma > 1/K$ ) implies that the mass transfer is from the top (bottom) gel-liquid interface to the bottom (top) gel-liquid interface.  $\gamma = 1/K$  implies that the gel-liquid interfaces are at equilibrium and there is no net mass transfer in the system. Marangoni stresses are absent in the base state as the concentration of the solute at the liquid-liquid interface is uniform in the flow direction.

The base state displacement fields  $U_{g,3}$  and  $U_{g,4}$  of the soft-gels are given, respectively, by

$$U_{g,3} = \frac{(y - n_{31})Wi_3(n_{21}(-4 + y + n_{31} + n_{21}(-3 + y + n_{31})) - \mu_{21})}{n_{21}(1 + n_{21})}, \quad (20)$$

$$U_{g,4} = \frac{(y + n_{41})Wi_4(n_{21}^2 + (1 + n_{21}(2 + y + n_{21}(2 + y + 2n_{21} - n_{41})) - n_{41}))\mu_{21}}{n_{21}(1 + n_{21})\mu_{21}}. \quad (21)$$

Here  $Wi_j = \frac{\mu_j U_0}{G_j d_1}$  is the Weissenberg number which is a measure of deformable nature of the soft-gel layers. The shear modulus  $G_j$  and viscosity  $\mu_j$  are of the soft-gel layer under consideration. A higher Weissenberg number implies a highly deformable soft-gel layer. When the Weissenberg number tends to zero, the soft-gel layers behave like rigid solids. Here  $n_{31} = \frac{d_3}{d_1}$  ( $n_{41} = \frac{d_4}{d_1}$ ) is the thickness ratio of top (bottom) neo-Hookean gel to "Fluid 1." The base state displacement fields in the gels are obtained by imposing no displacement at the rigid walls and continuity of tangential stresses at the top and bottom gel-liquid interfaces. From the base state deformations and pressure, we obtain the Cauchy stress tensor in the base state,

$$\Gamma_j = \begin{bmatrix} 1 + \left(\frac{dU_{g,j}}{dy}\right)^2 - P_{g,j} & \frac{dU_{g,j}}{dy} \\ \frac{dU_{g,j}}{dy} & 1 - P_{g,j} \end{bmatrix}. \quad (22)$$

The first normal stress difference is given by

$$(\Gamma_j)_{xx} - (\Gamma_j)_{yy} = \left(\frac{dU_{g,j}}{dy}\right)^2. \quad (23)$$

This difference in the first normal stress can have a significant effect on the system stability.

#### IV. LINEAR STABILITY ANALYSIS

We carry out a temporal linear stability analysis to study the stability of the base state. Infinitesimal disturbances (denoted by  $\hat{\cdot}$ ) are imposed on the base flow, which are given by

$$\begin{Bmatrix} u_j \\ v_j \\ p_j \end{Bmatrix} = \begin{Bmatrix} u_j^{ss} + \varepsilon \hat{u}_j \\ v_j^{ss} + \varepsilon \hat{v}_j \\ p_j^{ss} + \varepsilon \hat{p}_j \end{Bmatrix} \quad \text{where } j = 1, 2 \quad (24)$$

and

$$\begin{Bmatrix} x_j \\ y_j \\ p_{g,j} \end{Bmatrix} = \begin{Bmatrix} X_j + U_{g,j} + \varepsilon \hat{u}_{g,j} \\ Y_j + \varepsilon \hat{v}_{g,j} \\ p_{g,j}^{ss} + \varepsilon \hat{p}_{g,j} \end{Bmatrix} \quad \text{where } j = 3, 4. \quad (25)$$

The perturbation for the axial component of velocity  $u_j$ , for example, is of the form

$$\hat{u}_j = \bar{u}_j(y) \exp[ik(x - ct)]. \quad (26)$$

Here  $k$  is real and represents the wave number and  $c$  is a complex wave speed.  $\bar{u}_i$  is the amplitude of the disturbance and is obtained as the eigenfunction of a linearised eigen-value problem. The complex wave speed is given by  $c = c_R + ic_I$ . Here  $c_R$  and  $c_I$  represent the phase velocity and the growth rate of

the perturbations. The base state becomes temporally unstable when  $kc_I > 0$ .

The linearised governing equations (1)–(3) for the two fluids  $j = 1, 2$  are

$$iku_j + \frac{dv_j}{dy} = 0, \quad (27)$$

$$\frac{\text{Re}_1 \rho_{j1}}{\mu_{j1}} \left[ -ikcu_j + U_j iku_j + \frac{dU_j}{dy} v_j \right] = -ikp_j + \left[ \frac{d^2 u_j}{dy^2} - k^2 u_j \right], \quad (28)$$

$$\frac{\text{Re}_1 \rho_{j1}}{\mu_{j1}} \left[ -ikcv_j + U_j ikv_j \right] = -\frac{dp_j}{dy} + \left[ \frac{d^2 v_j}{dy^2} - k^2 v_j \right]. \quad (29)$$

The linearised species transport equation  $j = 1, 2$  is given by

$$\left[ ikcc_j + U_j ikc_j + \frac{dC_{j0}}{dy} v_j \right] = \frac{D_{j1}}{Pe} \left[ \frac{d^2 c_j}{dy^2} - k^2 c_j \right]. \quad (30)$$

The linearised equations for the soft-gel layers  $j = 3, 4$  are

$$iku_{g,j} + \frac{dv_{g,j}}{dy} + \frac{dU_{g,j}}{dy} (ikv_{g,j}) = 0, \quad (31)$$

$$\begin{aligned} -ikp_{g,j} + \frac{1}{Wi_j} \left[ \frac{d^2 u_{g,j}}{dy^2} - k^2 u_{g,j} - \frac{d^2 U_{g,j}}{dy^2} (iku_{g,j}) \right. \\ \left. + \frac{dU_{g,j}}{dy} \left( ik \frac{du_{g,j}}{dy} \right) + \frac{dU_{g,j}}{dy} (-k^2 v_{g,j}) \right] \\ + (-ikc) \left[ \frac{d^2 u_{g,j}}{dy^2} - k^2 u_{g,j} + \frac{dU_{g,j}}{dy} \left( \frac{d^2 v_{g,j}}{dy^2} - k^2 v_{g,j} \right) \right. \\ \left. + \frac{d^2 U_{g,j}}{dy^2} \frac{dv_{g,j}}{dy} \right] = 0, \quad (32) \end{aligned}$$

$$\begin{aligned} -\frac{dp_{g,j}}{dy} + \frac{1}{Wi_j} \left[ \frac{d^2 v_{g,j}}{dy^2} - k^2 v_{g,j} + \frac{dU_{g,j}}{dy} \left( ik \frac{dv_{g,j}}{dy} \right) \right. \\ \left. + \frac{d^2 U_{g,j}}{dy^2} (ikv_{g,j}) - \frac{dU_{g,j}}{dy} (k^2 u_{g,j}) \right] \\ + (-ikc) \left[ \frac{d^2 v_{g,j}}{dy^2} - k^2 v_{g,j} - \frac{d^2 U_{g,j}}{dy^2} (ikv_{g,j}) \right] = 0. \quad (33) \end{aligned}$$

The boundary conditions at the liquid-liquid interface<sup>15,31,32</sup> are described in the Appendix. The linearised boundary conditions, continuity of velocities and stresses at the top gel-liquid interface, are

$$u_1 + \frac{dU_1}{dy} v_{g,1} = -ikcu_{g,3} + \left[ ikcv_{s,3} \frac{dU_{g,3}}{dy} \right], \quad (34)$$

$$v_1 = -ikcv_{g,3}, \quad (35)$$

$$\frac{1}{\mu_{31}} \left[ \frac{du_1}{dy} + ikv_1 \right] = \frac{1}{Wi_3} \left[ \frac{du_{g,3}}{dy} + ikv_{g,3} - \frac{dU_{g,3}}{dy} (iku_{g,3}) \right] + (-ikc) \left[ \frac{du_{g,3}}{dy} + \frac{dU_{g,3}}{dy} \left( \frac{dv_{g,3}}{dy} \right) + ikv_{g,3} \right], \quad (36)$$

$$\begin{aligned} & (-\mu_{31}p_{g,3}) + p_1 + \frac{2\mu_{31}}{Wi_3} \left[ \frac{dv_{g,3}}{dy} + \frac{dU_{g,3}}{dy} (ikv_{g,3}) \right] \\ & + \mu_{31} \left[ (-ikc) \frac{2dv_{g,3}}{dy} \right] - \frac{2dv_1}{dy} = \frac{1}{Ca_{31}} k^2 v_{g,3}. \quad (37) \end{aligned}$$

Similar boundary conditions are imposed at the bottom gel-liquid interface.

The growth rate of the perturbations imposed depends on the parameters  $n_{21}$ ,  $n_{31}$ ,  $n_{41}$ ,  $\rho_{21}$ ,  $\mu_{21}$ ,  $\mu_{31}$ ,  $\mu_{41}$ ,  $Ca_{21}$ ,  $Ca_{31}$ ,  $Ca_{41}$ ,  $Wi_3$ ,  $Wi_4$ ,  $Re_1$ ,  $Pe$ ,  $K$ ,  $\gamma$ ,  $Ma$ , and  $k$  for our system. The definitions of these dimensionless parameters are given in Table I.

The linearised equations result in a generalised eigenvalue problem [Eq. (38)] for the growth rate  $kc_I$ ,

$$\mathbf{A}x = c\mathbf{B}x \quad (38)$$

These are solved numerically using a Chebyshev spectral analysis<sup>33</sup> based on collocation. The variables are expressed as Chebyshev polynomials. These expansions are substituted in the governing equations and are evaluated in the interior Gauss-Lobatto points and solved using Mathematica®. An energy budget analysis is carried out to get physical insights into different instabilities. The total energy in the perturbed state is obtained by taking the inner product of the vectorial form of Navier-Stokes equations with the velocity vector. A detailed derivation of the energy budget analysis is given in the [supplementary material](#).

## V. RESULTS

In this section, we focus on different instability modes predicted by our model for two-phase stratified flows through micro-channels made of soft materials represented by the neo-Hookean model. Experimental studies in the literature have focused on understanding the elasto-hydrodynamic coupling between the fluid and microchannels made of PDMS. First we analyze our model for single phase flows. The deformations of the PDMS microchannels when water is pumped have been captured experimentally.<sup>8</sup> This is used to validate results obtained from our model.

### A. Validation of results obtained from linear stability theory with experimental results for high Weissenberg numbers

We first compare the scaling laws obtained from the linear stability analysis with experiments in the literature for single phase flows through soft-PDMS tubes.<sup>8</sup> The Reynolds number for which the laminar flow becomes unstable was determined experimentally.<sup>8</sup> A Tollmien-Schlichting (TS) wave type instability arises in the flow due to shear generated in the bulk fluids at higher Reynolds numbers. The PDMS had a shear modulus of  $10^4$  Pa. The diameter of the micro-channels varied from 10 to 1000  $\mu\text{m}$ . The average velocity of the fluid varied from 0.08

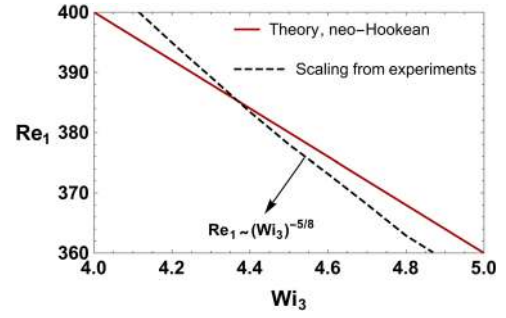


FIG. 2. Comparison of scaling of critical  $Re_1$  with  $Wi_3$  of experiments (solid line) and linear stability analysis (dashed line) based on the neo-Hookean model. The experiments predicted a scaling  $Re_1 \sim Wi_3^{-5/8}$  for single phase flow through pipes made of PDMS. This scaling is used to fit the data obtained from linear stability analysis. Other parameters are as follows:  $n_{21} = 1$ ,  $n_{31} = 1.5$ ,  $n_{41} = 1.5$ ,  $\mu_{21} = 1$ ,  $\mu_{31} = \mu_{41} = 10$ ,  $Ca_{21} = 0.001$ ,  $Ca_{31} = Ca_{41} = 0.001$ ,  $Wi_4 = 1$ .

to 0.8 m/s. The viscosity of the soft-gel ranged from 0.01 to 1 kg/m s. Under these conditions,  $Wi_3$  and  $Wi_4$  were in the range from 0.8 to 8. The experiments reveal that the critical  $Re_1$  at the onset of stability scaled according to  $Re_1 \sim Wi_3^{-5/8}$ . The predictions of the critical  $Re_1$  for  $Wi_3$  ranging from 4 to 5 follow this scaling, as shown in Fig. 2.

Our model also captures the scaling relationship in the limit of low  $Wi_3$  numbers and high  $Re_1$ , as seen in Fig. 3.

### B. Instabilities identified in the flow configuration

In this section, we discuss different instabilities each with distinct energy signatures that evolve in two-phase stratified flows. The analysis presented in this work considers two-phase flows where both phases are liquids. In pulmonary flows, we have a gas-liquid system with a high viscosity contrast. The results are presented in the form of dispersion curves and are interpreted physically using energy budget analysis. We consider an organic and an aqueous phase in our study. A typical soft-material could be PFA. Typical soluble surfactants could be SDS and SPAN80. Two-phase stratified flows in microchannels are generally observed for water (aqueous phase) and toluene/kerosene (organic phase). The typical physical properties of two-phase stratified flows of an organic and an aqueous phase are mentioned in Table IX. The ranges of dimensionless parameters obtained from the physical properties are given in Table X.

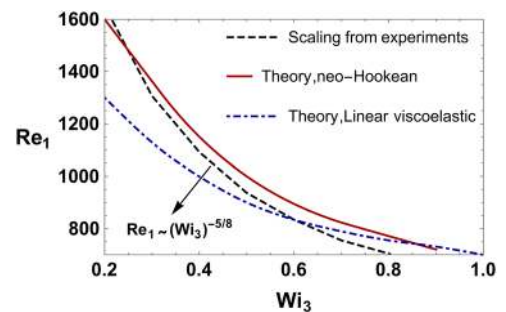


FIG. 3. Scaling analysis from experiments (dashed line) and linear stability analysis theory based on the neo-Hookean solid model (solid line) and linear viscoelastic model (dotted-dashed line).<sup>15</sup> Other parameters are as follows:  $n_{21} = 1$ ,  $n_{31} = 1.5$ ,  $n_{41} = 1.5$ ,  $\mu_{21} = 1$ ,  $\mu_{31} = \mu_{41} = 10$ ,  $Ca_{21} = 0.001$ ,  $Ca_{31} = Ca_{41} = 0.001$ ,  $Wi_4 = 0.1$ .

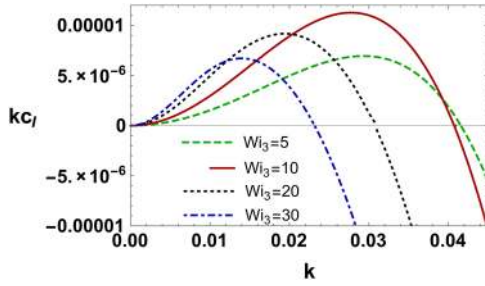


FIG. 4. Dispersion curves portraying the effect of neo-Hookean soft-gel layers on the liquid-liquid interfacial long wave instability (LW mode). Increasing  $Wi_3$  first destabilizes and then stabilises the system. Other parameters are as follows:  $n_{21} = 1.76$ ,  $n_{31} = 2$ ,  $n_{41} = 2$ ,  $\mu_{21} = 1.64$ ,  $\mu_{31} = \mu_{41} = 10$ ,  $Re_1 = 0$ ,  $Ca_{21} = 0.01$ ,  $Ca_{31} = 0.001$ ,  $Ca_{41} = 0.001$ ,  $Wi_4 = 0.5$ .

### 1. Instabilities in the absence of a soluble surfactant

We identify three important instabilities in the absence of soluble surfactants. An interfacial long wave (LW) instability arises in the flow due to the viscosity difference of the fluids at the liquid-liquid interface. We call this instability ‘‘LW’’ long wave instability. A Tollmien-Schlichting wave instability evolves in the flow due to shear generated in the bulk flow at high Reynolds numbers. This instability is referred as ‘‘TS’’ mode. An additional gel-liquid instability arises in the flow at the gel-liquid interface and is referred as ‘‘GL’’ mode.

*a. LW instability.* We first discuss the effect of the soft-gel layers on the liquid-liquid long wave (LW) interfacial instability. This instability arises in two-phase flows through rigid plates. To suppress TS mode which arises at high  $Re_1$ , we consider the creeping flow limit. The parameters used correspond to a typical organic-aqueous two-phase system. When a neo-Hookean solid model is used, the maximum growth rate first increases and then decreases with  $Wi_3$ , as shown in Fig. 4. This confirms the stabilizing influence of soft-gel layers for high  $Wi_3$ . To understand the dominant cause of the instability, an energy budget analysis is carried out. The results summarised in Table II show that the tangential stresses at the liquid-liquid interface dominate and cause this instability. This instability is attributed to a jump in the slope of the base state fluid velocities at the liquid-liquid interface. The streamline contour plots for this instability mode are shown in Fig. 5. These are denser at the liquid-liquid interface, confirming that the instability arises there. Our extensive numerical analysis for different parameters confirms that the soft-gel layers stabilize the LW mode for high  $Wi_3$ .

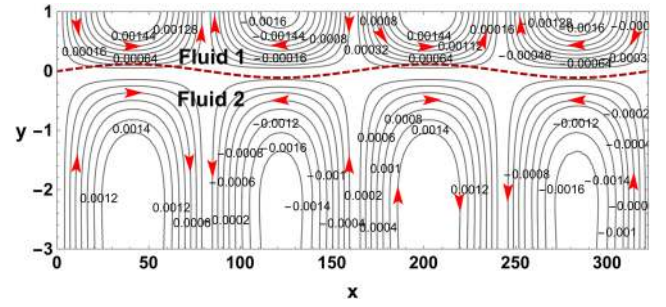


FIG. 5. Streamline contours for the LW mode. The perturbed interface is shown as the dashed line. Other parameters ( $Wi_3 = 20$ ) are the same as in Fig. 4.

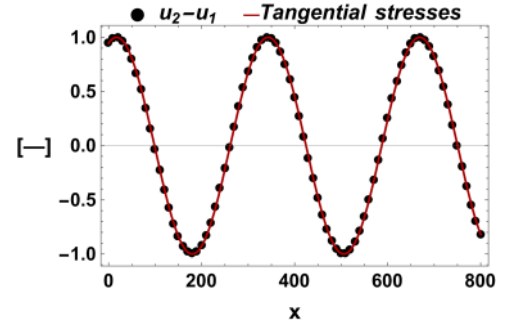


FIG. 6. Variation of normalised relative velocity of Fluid 1 with respect to Fluid 2 and the tangential stresses as a function of  $x$ . They are normalised with the maximum of their absolute values. Other parameters ( $Wi_3 = 20$ ) are the same as in Fig. 4.

Figure 6 shows the relative interfacial velocity of Fluid 1 with respect to Fluid 2 and the interfacial tangential stresses as a function of  $x$ . These are in phase at the liquid-liquid interface. This indicates that the tangential stresses at the crest pull the interface upward, and at the trough, the stresses pull the interface downward leading to an amplification of LW instability.

The LW instability evolved in the presence of soft-gel layers is physically visualised by plotting the eigenfunctions of the axial component of velocity at  $x = 2\pi/k$  and  $3\pi/k$ , as shown in Fig. 7. The gel-liquid and liquid-liquid interface deformation is also shown. The liquid-liquid interface deformation is amplified by the perturbed velocity in the fluids. The less viscous Fluid 1 is pushed away from the crest, and the more viscous Fluid 2 moves toward the crest at  $x = 200$ . This motion of the fluids pulls the liquid-liquid interface upward leading to destabilization of the LW instability. This velocity field physically explains the evolution of LW instability in the system.

TABLE II. Summary of the energy budget analysis for LW instability. The tangential stresses at the liquid-liquid interface are the dominant cause. Other parameters are the same as in Fig. 4. The boldface values represent the dominant cause of instability.

$Wi_3/k$	$\sum_{j=1}^2 E_{KE,j}$	$\sum_{j=1}^2 E_{REY,j}$	$E_{TAN,1}$	$E_{TAN,2}$	$E_{TAN,3}$	$E_{NOR,1}$	$E_{NOR,2}$	$E_{NOR,3}$	$\sum_{j=1}^4 E_{DIS,j}$
5/0.029	0	0	<b>0.986</b>	<b>0.011</b>	0	0	0.001	0	-1
10/0.027	0	0	<b>0.981</b>	<b>0.017</b>	0	0	0.001	0	-1
20/0.03	0	0	<b>0.979</b>	<b>0.02</b>	0	0	0.001	0	-1
30/0.013	0	0	<b>0.979</b>	<b>0.021</b>	0	0	0	0	-1

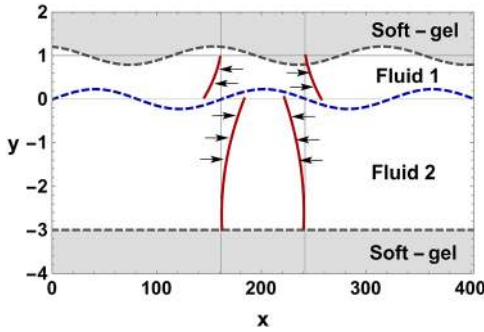


FIG. 7. Axial velocity field and interface position of the deformed state in LW mode. Other parameters are as follows:  $n_{21} = 3, n_{31} = 3, n_{41} = 4, \mu_{21} = 1.64, \mu_{31} = \mu_{41} = 10, Re_1 = 0, Ca_{21} = 0.01, Ca_{31} = 0.001, Ca_{41} = 0.001, Wi_4 = 0.5, Wi_3 = 5$ . The solid lines indicate the perturbed axial components of velocity in “Fluid 1” and “Fluid 2.” The arrows indicate the direction of motion of the fluids. The liquid-liquid, top, and bottom gel-liquid interface deformations are given by the dashed line.

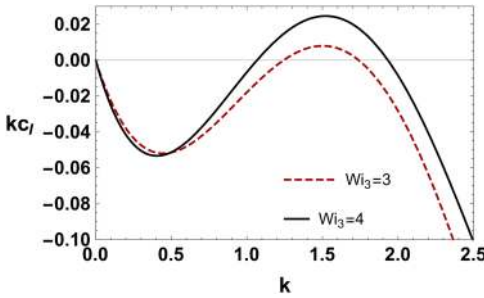


FIG. 8. Dispersion curves portraying the effect of  $Wi_3$  on the shear instability. Other parameters are as follows:  $n_{21} = 1, n_{31} = 1.5, n_{41} = 1.5, \mu_{21} = 1.64, \mu_{31} = \mu_{41} = 10, Re_1 = 1000, Ca_{21} = 0.01, Ca_{31} = 0.001, Ca_{41} = 0.001, Wi_4 = 1$ .

*b. TS instability.* TS instability is caused by the shear generated in the bulk fluids at high Reynolds numbers. At lower Reynolds numbers, this instability is not seen. In Fig. 8, we

show the dispersion curves of TS instability for two-phase flows through soft-gel coated walls. With an increase in  $Wi_3$ , the maximum growth rate of the perturbation increases and becomes positive. This indicates a destabilizing effect of soft-gels on the TS mode. This instability is physically explained by the dominant Reynolds stress term in the energy budget analysis in Table III. When we increase  $Wi_3$  from 3 to 4, the energy contributions from tangential stresses change from negative to positive. To summarise, the top soft-gel layer has a destabilizing effect on the TS mode. To get a better physical understanding of this instability, the stream function contour plots are obtained from the eigenfunctions corresponding to the maximum growth rate. In Fig. 9, the contours are denser in the bulk of the less viscous fluid confirming that this instability arises in this fluid due to high shear generated at large Reynolds numbers. The axial velocity line plots along the transverse direction in Fig. 10 show that the velocity is maximum in the less viscous Fluid 1. These perturbed axial components are obtained from the eigenfunctions corresponding to the maximum growth rate. The eigenfunctions are obtained by solving the generalised eigenvalue numerically. The TS mode evolves in the bulk of the fluids at higher Reynolds numbers due to shear generated in the fluids. So the perturbed velocity is maximum in the bulk of the less viscous fluid. This confirms the dominant role of the shear generated in the bulk of Fluid 1 in the evolution of TS instability.

The neutral stability curves of the system are shown in Fig. 11. Disturbances with Weissenberg numbers less than the critical Weissenberg decay and the TS instability are stabilized in the flow. Disturbances with Weissenberg numbers more than the critical value lead to the evolution of TS instability in the flow.

*c. GL instability.* A GL instability arises at the gel-liquid interface due to the deformable nature of the soft-gel.

TABLE III. Energy budget analysis for TS instability shown in Fig. 8. Reynolds stresses dominate in the energy budget analysis. The boldface values represent the dominant cause of instability.

$Wi_3/k$	$E_{KE}$	$E_{REY}$	$E_{TAN,1}$	$E_{TAN,2}$	$E_{TAN,3}$	$E_{NOR,1}$	$E_{NOR,2}$	$E_{NOR,3}$	$\sum_{j=1}^4 E_{DIS,j}$
3/1.45	0.17	<b>1.15</b>	0.005	-0.003	-0.017	-0.018	0	-0.005	-1
4/1.5	0.375	<b>1.335</b>	0.004	0.093	-0.012	-0.041	0.003	-0.004	-1

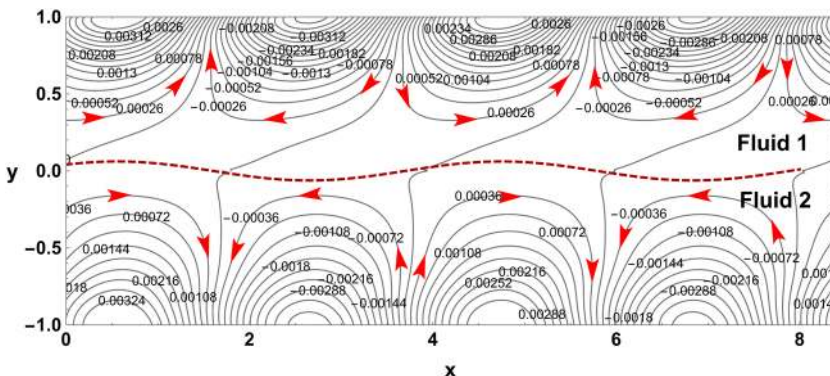


FIG. 9. Stream contour plot for the TS mode shown in Fig. 8. The contours are denser in the bulk of Fluid 1 which is less viscous. Other parameters are the same, as shown in Fig. 8. The plot is at fixed time. At different times, the qualitative trends are preserved.

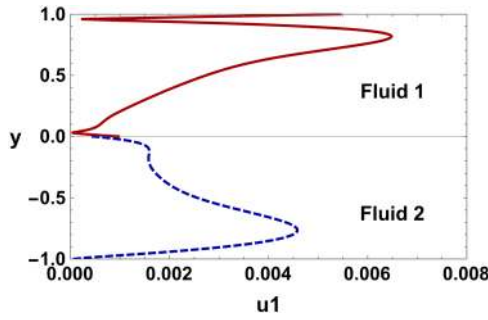


FIG. 10. Variation of the axial component of velocity at the liquid-liquid interface along the transverse direction. Other parameters are the same, as shown in Fig. 8.

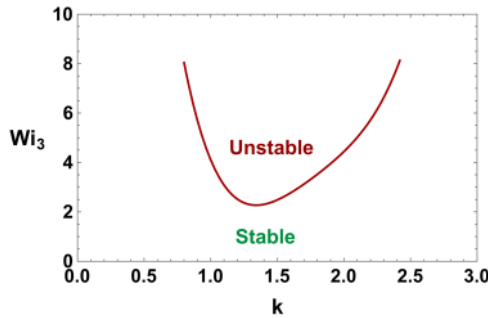


FIG. 11. Neutral stability curves for TS mode depicted in Fig. 8 showing stable and unstable regions. Other parameters are the same, as shown in Fig. 8.

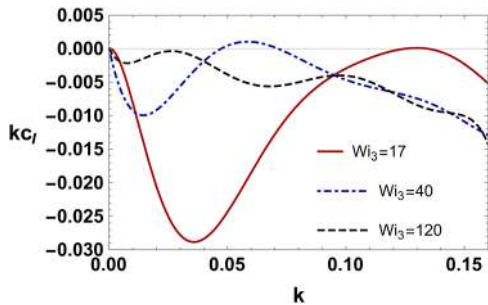


FIG. 12. Dispersion curves for the gel-liquid instability. Arrow points in the direction of increasing  $Wi_3$ . Other parameters are as follows:  $n_{21} = 1$ ,  $n_{31} = n_{41} = 4$ ,  $\mu_{21} = 1.09$ ,  $\mu_{31} = \mu_{41} = 10$ ,  $Re_1 = 1$ ,  $Ca_{21} = 0.001$ ,  $Ca_{31} = Ca_{41} = 0.001$ ,  $Wi_4 = 0.001$ .

In Fig. 12, with an increase in  $Wi_3$ , first a destabilization and then a stabilization of GL instability which originates from the top gel-liquid interface are observed. The viscosity ratio is chosen close to 1 and the Reynolds number is chosen low to suppress the LW and TS instabilities. This instability arises from the difference in the first normal stresses in the base state displacement field of the soft-gel when a neo-Hookean model

is used. The energy budget analysis shown in Table IV reveals that the tangential stresses at the top gel-liquid interface make a dominant contribution to instability. To obtain further insights into the physical mechanism that causes the GL instability, stream function contours are shown in Fig. 13. The streamlines are denser at the top gel indicating that this instability emanates from there. To summarise, the GL instability is stabilised by the deformable nature of the neo-Hookean soft-gel layers.

To get a better understanding on the stability of the GL mode, the neutral stability curve in the  $Wi_3$ - $k$  plane is determined and depicted in Fig. 14. Disturbances become unstable, when  $Wi_3$  lies between  $(Wi_3)_{\min}$  and  $(Wi_3)_{\max}$ . For low  $Wi_3$ , the soft-gel layers act like a rigid solid and the GL mode is stable. With an increase in  $Wi_3$ , the top gel-liquid interface deforms and gives rise to the GL mode. For very high  $Wi_3$ , the GL mode is stabilised by the deformable nature of the soft-gel.

## 2. Liquid-liquid interfacial instabilities in the presence of soluble surfactants

We now analyze the role of Marangoni stresses induced by the presence of soluble surfactants on the stability of stratified flows. We identify three important instabilities in the presence of soluble surfactants. An interfacial instability arises in the flow due to the viscosity difference at the liquid-liquid interface. This is similar to the ‘‘LW’’ long wave instability observed in Sec. V B 1. Another interfacial instability arises in the flow due to Marangoni effects and is called ‘‘MLW’’ Marangoni long wave instability. A liquid-liquid short wave instability evolves in the flow due to the presence of soluble surfactants. We refer to this instability as ‘‘SW’’ mode. The focus of this section is on the evolution of interfacial instabilities due to surfactants. Here we do not investigate the instabilities that arise due to shear in the bulk fluids and at the gel-liquid interface.

*a. LW and MLW instability modes.* The long wave ‘‘LW’’ instability mode seen in the presence of a soluble surfactant is similar to that shown in Sec. V B 1. The energy signatures, the physical cause, and the effect of soft-gel-layers on the instability are also identical as in the case of no surfactant. This is seen for low Marangoni numbers.

Another long wave mode arises due to gradients in the  $y$ -direction in the base state concentration field. This results in non-uniform surface tension when the liquid-liquid interface is perturbed. This creates Marangoni effects at the liquid-liquid interface which leads to the evolution of this instability. When the direction of mass transfer is from the less viscous

TABLE IV. Energy budget analysis for GL instability shown in Fig. 12. Tangential stresses at the top gel-liquid interface dominate the energy balance equation. The boldface values represent the dominant cause of instability.

$Wi_3/k$	$\sum_{j=1}^2 E_{KE,j}$	$\sum_{j=1}^2 E_{REY,j}$	$E_{TAN,1}$	$E_{TAN,2}$	$E_{TAN,3}$	$E_{NOR,1}$	$E_{NOR,2}$	$E_{NOR,3}$	$\sum_{j=1}^4 E_{DIS,j}$
20/0.1	0	0	0.004	<b>1.052</b>	0	0	-0.054	0	-1
40/0.06	0	0	0	<b>1.042</b>	0	0	-0.047	0	-1

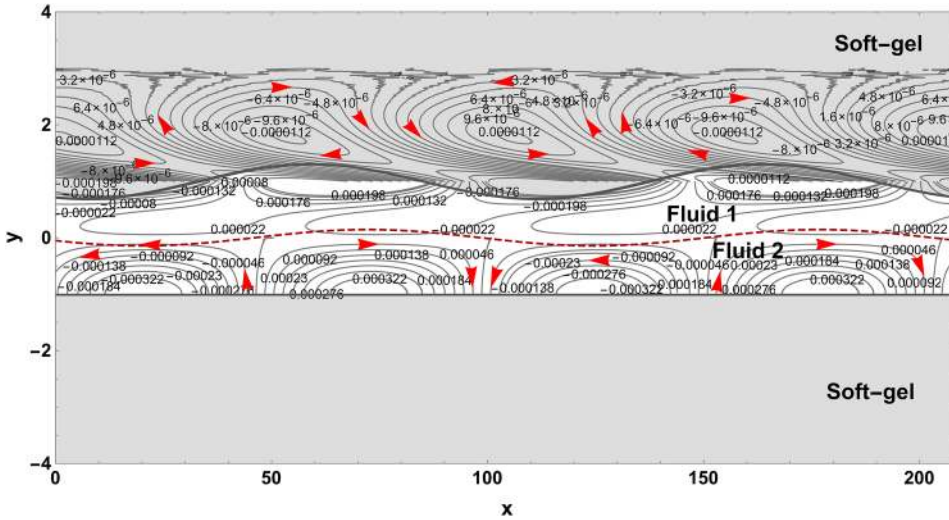


FIG. 13. Streamline plot for GL instability shown in Fig. 12. The contours are denser near the top gel-liquid interface indicating that the GL instability evolves at this interface. Other parameters ( $Wi_3 = 40$ ) are the same, as shown in Fig. 12.

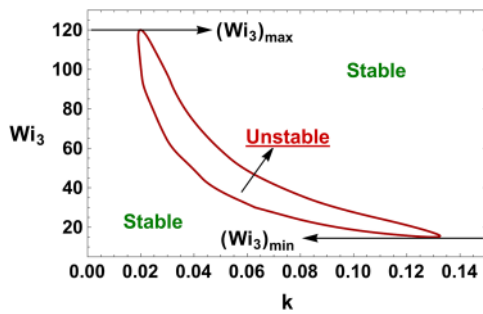


FIG. 14. Neutral stability curve for the gel-liquid instability shown in Fig. 12. Other parameters the same as in Fig. 12.

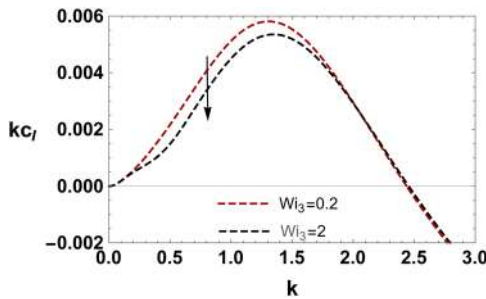


FIG. 15. Dispersion curves for the MLW mode. Other parameters are as follows:  $n_{21} = 1.5$ ,  $n_{31} = 2$ ,  $n_{41} = 2$ ,  $\mu_{21} = 1.64$ ,  $\mu_{31} = \mu_{41} = 10$ ,  $\gamma = 0.5$ ,  $K = 0.5$ ,  $D_{21} = 0.5$ ,  $Re_1 = 0$ ,  $Pe = 2000$ ,  $Ca_{21} = 100$ ,  $Ca_{31} = 0.001$ ,  $Ca_{41} = 0.001$ ,  $Wi_4 = 0.2$ ,  $Ma = 12000$ .

“Fluid 1” to more viscous “Fluid 2,” the LW mode transforms into an MLW instability mode. The stabilizing effect of soft-gel-layers on the MLW instability is shown in Fig. 15. When

$Wi_4$  increases from 0.2 to 2, the MLW mode is stabilized by the deformable nature of the soft-gel. The energy budget analysis shown in Table V confirms the dominance of first Marangoni stresses as the primary cause of this instability. The stabilization of MLW mode is attributed to the reduction in the magnitude of tangential stresses with the deformable nature of the soft-gel layers. To summarise, the direction of mass transfer plays a crucial role in dictating whether the instability is LW or MLW. For  $\gamma > 1/K$  tangential stresses and for  $\gamma < 1/K$ , first Marangoni stresses primarily contribute to the LW and MLW mode observed. When the mass transfer is from the more viscous fluid to the less viscous fluid, LW instability arises in the system. When the direction of mass transfer is from the less viscous fluid to the more viscous fluid, MLW instability evolves in the system. The neo-Hookean soft-gel layers stabilise both the modes as the deformability increases.

Figure 16 shows the interface deformation and the first Marangoni stresses at the liquid-liquid interface. The first Marangoni stresses are a primary cause of instability and are in phase with the interface deformation. These stresses arise due to base state concentration gradients in the transverse direction. These stresses and displacement are maximum (minimum) at  $x = 13$  ( $x = 16$ ). The first Marangoni stresses are positive at the crest and negative at the trough causing an amplified interface resulting in an MLW instability.

*b. SW instability mode.* The Marangoni effects at the liquid-liquid interface lead to the evolution of a SW instability. This instability evolves at low  $Re_1$  and high  $Ma$ . The perturbed concentration gradients along the flow direction result in different concentrations of the solute at the crest and trough

TABLE V. Energy budget analysis for the MLW instability shown in Fig. 15. First Marangoni stresses at the liquid-liquid dominate the energy budget analysis. Other parameters are the same, as shown in Fig. 15. The boldface values represent the dominant cause of instability.

$Wi_3/k$	$E_{MAS,I}$	$E_{MAS,F}$	$E_{TAN,1}$	$E_{TAN,2}$	$E_{TAN,3}$	$E_{NOR,1}$	$E_{NOR,2}$	$E_{NOR,3}$	$\sum_{j=1}^4 E_{DIS,j}$
0.2/1.29	<b>2.823</b>	-1.935	0.111	0.001	0.002	-0.001	0	-0.001	-1
2/1.33	<b>2.879</b>	-2	0.122	-0.002	0.002	-0.001	0	0	-1

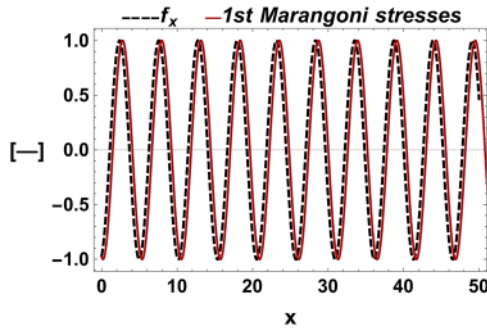


FIG. 16. Variation of normalised first Marangoni stresses and normalised gradients of the interface deformation in the axial direction. They are normalised with the maximum of their absolute values. Other parameters ( $Wi_4 = 2$ ) are the same, as shown in Fig. 15.

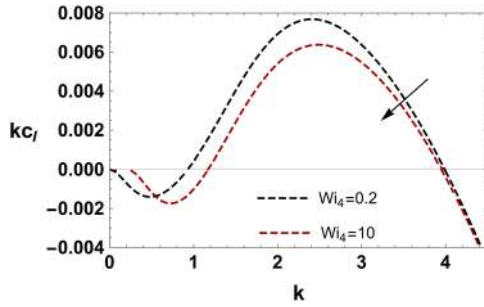


FIG. 17. Dispersion curves showing the stabilization of the SW mode with an increase in  $Wi_4$ . The arrow points in the direction of increasing  $Wi_4$ . Other parameters are as follows:  $n_{21} = 0.9$ ,  $n_{31} = 2$ ,  $n_{41} = 3$ ,  $\mu_{21} = 1.64$ ,  $\mu_{31} = \mu_{41} = 10$ ,  $\gamma = 0.5$ ,  $K = 0.5$ ,  $D_{21} = 0.5$ ,  $Re_1 = 0$ ,  $Pe = 2000$ ,  $Ca_{21} = 100$ ,  $Ca_{31} = 0.001$ ,  $Ca_{41} = 0.001$ ,  $Wi_3 = 0.2$ ,  $Ma = 12\ 000$ .

of the deformed interface. This leads to gradients of surface tension at the liquid–liquid interface which causes a SW instability. In Fig. 17, we show that with an increase in  $Wi_4$ , the growth rate of the perturbation decreases. The energy analysis shown in Table VI confirms that the second Marangoni stress term dominates the energy balance. The stabilization of SW mode with an increase in the deformable nature of the gel is physically explained using energy budget analysis. Energy budget analysis reveals that, for the SW mode, the second Marangoni stresses dominate. The stabilization of this mode is attributed to the reduction in the magnitude of the second Marangoni stress energy term with an increase in  $Wi_4$  from 0.2 to 10. This is explained by physically visualising the perturbed axial components of velocity of the fluids at  $x = \frac{2\pi}{k}$  and  $x = \frac{3\pi}{k}$ , as shown in Fig. 18. The less viscous Fluid 1 is driven toward the crest of the liquid–liquid interface and the more viscous Fluid 2 is driven away from the crest of the liquid–liquid interface. This motion of the fluids results in suppressing the deformation of the liquid–liquid interface and the stabilization of MLW instability.

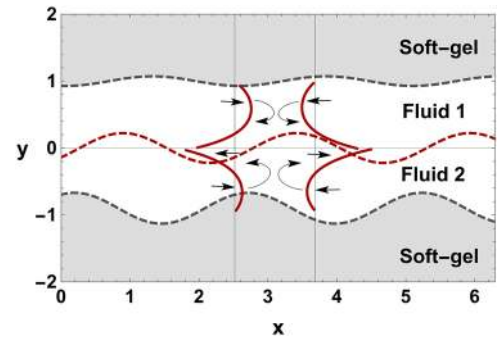


FIG. 18. Axial velocity field and interface position of the deformed state in SW mode. The perturbed axial component of velocity of the fluids is shown as the solid line. Deformations of the liquid–liquid interface and top and bottom gel–liquid interfaces are shown as the dashed line. The deformation of the liquid–liquid interface and bottom gel–liquid interface show phase lag. Other parameters are ( $Wi_4 = 10$ ) the same, as shown in Fig. 17.

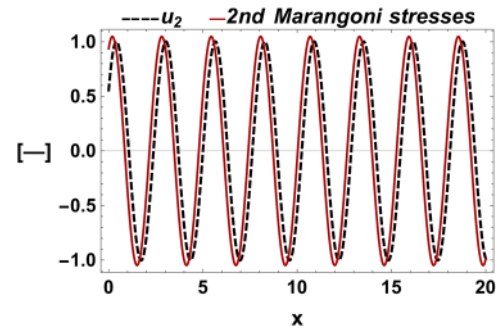


FIG. 19. Variation of normalised second Marangoni stresses and normalized Fluid 2 velocity in the axial direction. They are normalised by the maximum of their absolute values. Other parameters are ( $Wi_4 = 10$ ) the same, as shown in Fig. 17.

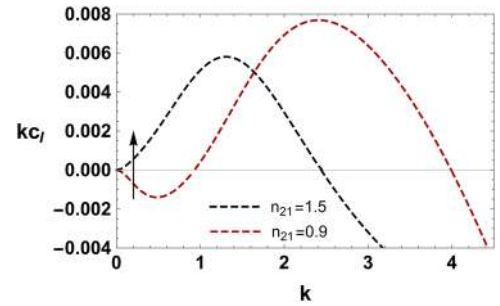


FIG. 20. Transition of the SW mode to LW mode with an increase in the thickness ratio  $n_{21}$  is shown. Arrow points in the direction of increasing  $n_{21}$ . Other parameters are as follows:  $n_{31} = 2$ ,  $n_{41} = 3$ ,  $\mu_{21} = 1.64$ ,  $\mu_{31} = \mu_{41} = 10$ ,  $\gamma = 0.5$ ,  $K = 0.5$ ,  $D_{21} = 0.5$ ,  $Re_1 = 0$ ,  $Pe = 2000$ ,  $Ca_{21} = 100$ ,  $Ca_{31} = 0.001$ ,  $Ca_{41} = 0.001$ ,  $Wi_3 = 0.2$ ,  $Wi_4 = 10$ ,  $Ma = 12\ 000$ .

To physically understand the evolution of SW instability, we plot the normalised second Marangoni stresses and Fluid 2 velocity at the liquid–liquid interface along the axial

TABLE VI. Energy budget analysis for SW mode shown in Fig. 17. Second Marangoni stresses dominate the energy balance. Other parameters are the same, as shown in Fig. 17. The boldface values represent the dominant cause of instability.

$Wi_4/k$	$E_{MAS,I}$	$E_{MAS,F}$	$E_{TAN,1}$	$E_{TAN,2}$	$E_{TAN,3}$	$E_{NOR,1}$	$E_{NOR,2}$	$E_{NOR,3}$	$\sum_{j=1}^4 E_{DIS,j}$
0.2/0.23	-0.277	<b>1.186</b>	0.089	0	0.002	0	0	0	-1
10/2.49	-0.076	<b>1.15</b>	-0.064	0	-0.01	0	0	0	-1

TABLE VII. Energy budget analysis for SW to MLW transition shown in Fig. 20. Energy signature changes from second Marangoni stresses to first Marangoni stresses dominating the energy budget with an increase in  $n_{21}$ . Other parameters are the same, as shown in Fig. 20. The boldface values represent the dominant cause of instability.

$n_{21}/k$	$E_{MAS,I}$	$E_{MAS,F}$	$E_{TAN,1}$	$E_{TAN,2}$	$E_{TAN,3}$	$E_{NOR,1}$	$E_{NOR,2}$	$E_{NOR,3}$	$\sum_{j=1}^4 E_{DIS,j}$
0.9/0.23	-0.277	<b>1.186</b>	0.089	0	0.002	0	0	0	-1
1.5/1.21	<b>2.821</b>	-1.934	0.111	0.001	0.002	-0.001	0	0	-1

direction in Fig. 19. The second Marangoni stresses the primary cause of the instability are in phase with the Fluid 2 velocity, indicating that they drag the fluid up near the crests and down near the troughs. This motion of the fluid results in an amplified deformation of the liquid-liquid interface and evolution of SW instability.

The SW mode shows a transition to MLW mode with an increase in the thickness ratio of the fluids  $n_{21}$ . This is shown in Fig. 20. For  $n_{21} = 0.9$ , SW mode of instability prevails in the flow, and for  $n_{21} = 1.5$ , MLW mode becomes unstable. This transition is physically analyzed using energy budget analysis shown in Table VII. The energy signature changes from second Marangoni stresses dominating for SW to first Marangoni stresses dominating for MLW with an increase in  $n_{21}$ . The SW mode changes to MLW mode with an increase in the thickness ratio of the fluids  $n_{21}$ .

## VI. CONCLUSIONS

This work focuses on the importance of using a neo-Hookean model to represent the soft material. We use the Eulerian formulation proposed in Ref. 25. This formulation changes the dynamics of elastohydrodynamic coupling between the soft-gel-layers and the fluids. In this model, there is a difference in the first normal stresses in the base state displacement field of the neo-Hookean soft-gel. This leads to an instability behavior which is significantly different from that predicted by a linear viscoelastic model.<sup>15,32</sup> In Sec. V B 1 of the paper, we looked into the effect of neo-Hookean soft-gel layers on different instabilities that arise in the flow. In Sec. V B 2, the focus is on analyzing the combined effect of neo-Hookean soft-gel layers and soluble surfactants on different instabilities that evolve in the flow. Insights into the physical mechanism driving different instabilities are obtained by carrying out an energy budget analysis of the perturbed flow.

We first validated the model with single phase experiments. We then analyzed numerically two types of two-phase stratified flow configurations (a) in the absence of a soluble

surfactant and (b) in the presence of soluble surfactants. We identified three crucial instabilities LW, TS, and GL modes in the absence of soluble surfactants. The LW mode evolves in the flow due the viscosity differences of the fluids at the liquid-liquid interface. To our surprise, from our extensive numerical analysis, we observe that this mode is always stabilised by the presence of neo-Hookean soft-gel layers for high Weissenberg numbers. An energy budget analysis indicates that the tangential stresses at the liquid-liquid interface dominate and cause the instability.

Next we analyzed the effect of neo-Hookean soft-gel-layers on the TS mode. This work shows destabilization of TS mode when a neo-Hookean model is used. Energy budget analysis indicates that this mode arises in the flow due to Reynolds stresses generated in the bulk fluids. The destabilization of this mode is attributed to the tangential stresses at the gel-liquid interface.

A new GL instability arises at the gel-liquid interface due to the deformable nature of the soft-gel. This instability arises in the flow due to a sudden jump in the shear modulus of the soft-gels at the gel-liquid interface. This is indicated by the dominance of the tangential stresses at the gel-liquid interface in the energy budget analysis. The stabilization of GL instability is attributed to the reduction in the magnitude of tangential stresses at the gel-liquid interface as the deformable nature of the soft-gel increases.

We further investigate the flow configuration in the presence of soluble surfactants. Here three distinct instabilities are identified, LW, MLW, and SW modes. When the direction of mass transfer is from the bottom to top gel-liquid interface, LW mode arises. This mode is stabilised by the neo-Hookean soft-gel layers for large Weissenberg numbers. When the direction of mass transfer is from the top to bottom gel-liquid interface, LW mode evolves as MLW mode. Our extensive numerical analysis indicates that MLW mode is stabilised by the deformable nature of neo-Hookean soft-gel layers. This instability mode is physically explained by the dominance of first Marangoni stresses at the liquid-liquid

TABLE VIII. Conditions for the occurrence of different instabilities that arise in two-phase flows through soft-gel-coated walls.

Type of instability	Effect of increasing			Dominant cause
	Weissenberg number	Reynolds number	Marangoni number	
LW mode	Stabilization	Low	Low	Viscosity difference
TS mode	Destabilization	High	Low	Shear generated in the bulk of the fluids
GL mode	Stabilization	Low	Low	Deformability of the soft-gel
MLW mode	Stabilization	Low	High	Changes in surface tension due to the presence of soluble surfactants
SW mode	Stabilization	Low	High	Changes in surface tension due to the presence of soluble surfactants

interface in the energy budget analysis. This is caused by the gradients in the base state concentration field in the transverse direction. This causes concentration and surface tension gradients along the deformed interface. This leads to an evolution of SW mode. This mode changes into MLW mode by decreasing the fluid thickness ratio. Energy analysis indicates that the SW mode arises due to the domination of the second Marangoni stress term. Conditions under which different instabilities are observed are given in Table VIII.

To summarise, in most cases, stabilization is achieved by the deformable nature of neo-Hookean soft-gel layers, as shown in Table VIII. An important task for the future is to include the dependency of the perturbations in the z-direction<sup>34</sup> and to perform a non-modal analysis for the stability.<sup>35</sup>

## SUPPLEMENTARY MATERIAL

A detailed derivation of the energy budget analysis is given in the [supplementary material](#). The total energy in the perturbed state is obtained by taking the inner product of the vectorial form of Navier-Stokes equations with the velocity vector.

## APPENDIX: BOUNDARY CONDITIONS AND PHYSICAL PARAMETERS

### 1. Boundary conditions at the liquid-liquid interface

The boundary conditions at the perturbed liquid-liquid interface in the absence of soluble surfactant

$$y = f(x, t) = \varepsilon \delta \exp[ik(x - ct)] \quad (\text{A1})$$

are obtained using domain perturbation. Here  $\delta$  is the amplitude of the perturbed liquid-liquid interface. The continuity of

velocity yields

$$u_1 + \frac{dU_1}{dy} \delta = u_2 + \frac{dU_2}{dy} \delta, \quad (\text{A2})$$

$$v_1 = v_2. \quad (\text{A3})$$

The continuity of shear stress gives

$$\frac{du_1}{dy} + ikv_1 = \mu_{21} \left( \frac{du_2}{dy} + ikv_2 \right). \quad (\text{A4})$$

The normal stress boundary condition yields

$$(\mu_{21} p_2 - p_1) + 2 \frac{dv_1}{dy} - 2\mu_{21} \frac{dv_2}{dy} = \frac{1}{Ca_{21}} k^2 \delta, \quad (\text{A5})$$

where  $Ca_{21} = \frac{\mu_1 U_{10}}{\sigma_0}$ . The kinematic boundary condition yields

$$\delta(ikc - U_1 ik) + v_1 = 0. \quad (\text{A6})$$

Boundary conditions at the liquid-liquid interface in the presence of soluble surfactants are given by

$$c_1 = 1 \quad \text{at } y = 1 + g(x, t), \quad (\text{A7})$$

$$c_2 = \frac{C_{20}}{C_{10}} = \gamma \quad \text{at } y = -n_{21} + h(x, t), \quad (\text{A8})$$

$$c_1 = K c_2 \quad \text{at } y = f(x, t), \quad (\text{A9})$$

$$-\partial_x f \partial_x c_1 + \partial_y c_1 = D_{21} \left( -\partial_x f \partial_x c_2 + \partial_y c_2 \right) \quad \text{at } y = f(x, t), \quad (\text{A10})$$

$$\mu_{21} p_2 - p_1 - \left( 2\mu_{21} \frac{\partial v_2}{\partial y} \right) + 2 \frac{\partial v_1}{\partial y} = \frac{-1}{Ca_{21}} \frac{\partial^2 f}{\partial x^2}. \quad (\text{A11})$$

### 2. Parameters for the two-phase systems considered in this work

TABLE IX. The range of physical properties of organic-aqueous two-phase stratified flows prevailing in microchannel experiments.

S. No	Physical property	Range
1	Density of aqueous phase	1000 kg/m <sup>3</sup>
2	Density of organic phase	800–900 kg/m <sup>3</sup>
3	Viscosity of aqueous phase	0.001 kg/m s
4	Viscosity of organic phase	0.0005–0.002 kg/m s
5	Viscosity of PFA	0.02–1 kg/m sec
6	Dimensions of the micro-channel	100 $\mu$ m $\times$ 100 $\mu$ m
7	Flowrate of aqueous phase	1200 $\mu$ l/h
8	Shear modulus of PFA	10–600 kPa
9	Surface tension between the organic-aqueous interface in the presence of SDS	10–40 mN/m
10	Surface tension between the aqueous phase-PFA interface	19.1 mN/m
11	Surface tension between the organic phase-PFA interface	20–40 mN/m
12	Diffusivity of SDS in aqueous phase	$0.06 \times 10^{-10}$ m <sup>2</sup> /s
13	Diffusivity of SDS in organic phase	$0.06\text{--}1.2 \times 10^{-11}$ m <sup>2</sup> /s
14	Variation of interfacial tension with concentration ( $\sigma_0 \beta$ )	$O(10^{-6})$ Nm <sup>2</sup> /mol

TABLE X. Dimensionless quantities for organic-aqueous two-phase stratified flows in microchannel experiments.

S. No	Dimensionless quantity	Range
1	Viscosity ratio of organic to aqueous phase	0.5–2
2	Viscosity ratio of PFA to aqueous phase	20–300
3	Density ratio of organic phase to aqueous phase	0.81
4	Reynolds number	0–3
5	Weissenberg number of PFA	0.028–100
6	Capillary number at the organic-aqueous phase interface	$0.0015 O(10^{-3})$
7	Capillary number at the PFA-aqueous phase interface	$O(10^{-3})$
8	Capillary number at the PFA-organic phase interface	$O(10^{-3})$
9	Marangoni number for the organic-aqueous phase interface	$O(10^3)–O(10^4)$

- <sup>1</sup>T. M. Squires and S. R. Quake, “Microfluidics: Fluid physics at the nanoliter scale,” *Rev. Mod. Phys.* **77**, 977 (2005).
- <sup>2</sup>K. Ren, W. Dai, J. Zhou, J. Su, and H. Wu, “Whole-Teflon microfluidic chips,” *Proc. Natl. Acad. Sci. U. S. A.* **108**, 8162 (2011).
- <sup>3</sup>K. Ren, J. Zhou, and H. Wu, “Materials for microfluidic chip fabrication,” *Acc. Chem. Res.* **46**, 2396 (2013).
- <sup>4</sup>P. N. Nge, C. I. Rogers, and A. T. Woolley, “Advances in microfluidic materials, functions, integration, and applications,” *Chem. Rev.* **113**, 2550 (2013).
- <sup>5</sup>J. A. Moriarty and A. J. B. Grotberg, “Flow-induced instabilities of a mucous bilayer,” *J. Fluid Mech.* **397**, 1 (1999).
- <sup>6</sup>J. B. Grotberg and O. E. Jensen, “Biofluid mechanics in flexible tubes,” *Annu. Rev. Fluid Mech.* **36**, 121 (2004).
- <sup>7</sup>V. Kumaran and R. Muralikrishnan, “Spontaneous growth of fluctuations in the viscous flow of a fluid past a soft interface,” *Phys. Rev. Lett.* **84**, 3310 (2000).
- <sup>8</sup>M. K. S. Verma and V. Kumaran, “A dynamical instability due to fluid-wall coupling lowers the transition Reynolds number in the flow through a flexible tube,” *J. Fluid Mech.* **705**, 322 (2012).
- <sup>9</sup>M. Verma and V. Kumaran, “A multifold reduction in the transition Reynolds number, and ultra-fast mixing, in a micro-channel due to a dynamical instability induced by a soft wall,” *J. Fluid Mech.* **727**, 407 (2013).
- <sup>10</sup>M. K. S. Verma and V. Kumaran, “Stability of the flow in a soft tube deformed due to an applied pressure gradient,” *Phys. Rev. E* **91**, 043001 (2015).
- <sup>11</sup>R. Neelamegam, D. Giribabu, and V. Shankar, “Instability of viscous flow over a deformable two-layered gel: Experiments and theory,” *Phys. Rev. E* **90**, 043004 (2014).
- <sup>12</sup>V. Kumaran, “Stability of the viscous flow of a fluid through a flexible tube,” *J. Fluid Mech.* **294**, 259 (1995).
- <sup>13</sup>V. Kumaran, “Stability of fluid flow through a flexible tube at intermediate Reynolds number,” *J. Fluid Mech.* **357**, 123 (1998).
- <sup>14</sup>V. Shankar and L. Kumar, “Stability of two-layer Newtonian plane Couette flow past a deformable solid layer,” *Phys. Fluids* **16**, 4426 (2004).
- <sup>15</sup>B. Dinesh and S. Pushpavanam, “Linear stability of layered two-phase flows through parallel soft-gel-coated walls,” *Phys. Rev. E* **96**, 013119 (2017).
- <sup>16</sup>V. Shankar and A. K. Sahu, “Suppression of instability in liquid flow down an inclined plane by a deformable solid layer,” *Phys. Rev. E* **73**, 016301 (2006).
- <sup>17</sup>V. Gkanis and S. Kumar, “Instability of creeping flow past a deformable wall: The role of depth-dependent modulus,” *Phys. Rev. E* **73**, 026307 (2006).
- <sup>18</sup>V. Gkanis and S. Kumar, “Instability of creeping Couette flow past a neo-Hookean solid,” *Phys. Fluids* **15**, 2864 (2003).
- <sup>19</sup>V. Gkanis and S. Kumar, “Instability of gravity-driven free-surface flow past a deformable elastic solid,” *Phys. Fluids* **18**, 044103 (2006).
- <sup>20</sup>Gaurav and V. Shankar, “Stability of gravity-driven free-surface flow past a deformable solid at zero and finite Reynolds number,” *Phys. Fluids* **19**, 024105 (2007).
- <sup>21</sup>P. Chokshi and V. Kumaran, “Weakly nonlinear analysis of viscous instability in flow past a neo-Hookean surface,” *Phys. Rev. E* **77**, 056303 (2008).
- <sup>22</sup>Gaurav and V. Shankar, “Stability of fluid flow through deformable neo-Hookean tubes,” *J. Fluid Mech.* **627**, 291 (2009).
- <sup>23</sup>V. Gkanis and S. Kumar, “Stability of pressure-driven creeping flows in channels lined with a nonlinear elastic solid,” *J. Fluid Mech.* **524**, 357 (2005).
- <sup>24</sup>Gaurav and V. Shankar, “Stability of pressure-driven flow in a deformable neo-Hookean channel,” *J. Fluid Mech.* **659**, 318 (2010).
- <sup>25</sup>R. Patne, D. Giribabu, and V. Shankar, “Consistent formulations for stability of fluid flow through deformable channels and tubes,” *J. Fluid Mech.* **827**, 31 (2017).
- <sup>26</sup>S. Sahu and V. Shankar, “Passive manipulation of free-surface instability by deformable solid bilayers,” *Phys. Rev. E* **94**, 013111 (2016).
- <sup>27</sup>D. Chakraborty, J. R. Prakash, J. Friend, and L. Yeo, “Fluid-structure interaction in deformable microchannels,” *Phys. Fluids* **24**, 102002 (2012).
- <sup>28</sup>R. Neelamegam and V. Shankar, “Experimental study of the instability of laminar flow in a tube with deformable walls,” *Phys. Fluids* **27**, 024102 (2015).
- <sup>29</sup>C. W. Macminn, E. R. Dufresne, and J. S. Wettlaufer, “Large deformations of a soft porous material,” *Phys. Rev. Appl.* **5**, 044020 (2016).
- <sup>30</sup>S. G. Yiantsios and B. G. Higgins, “Linear stability of plane Poiseuille flow of two superposed fluids,” *Phys. Fluids* **31**, 3225 (1988).
- <sup>31</sup>J. R. Picardo, T. G. Radhakrishna, and S. Pushpavanam, “Solutoal Marangoni instability in layered two-phase flows,” *J. Fluid Mech.* **793**, 280 (2016).
- <sup>32</sup>B. Dinesh and S. Pushpavanam, “Effect of soluble surfactants on the stability of stratified flows through soft-gel-coated walls,” *Phys. Rev. E* **98**, 023106 (2018).
- <sup>33</sup>P. A. M. Boomkamp, B. J. Boersma, R. H. M. Miesen, and G. V. Beijnon, “A Chebyshev collocation method for solving two-phase flow stability problems,” *J. Comput. Phys.* **132**, 191 (1997).
- <sup>34</sup>M. H. Allouche, S. Millet, V. Botton, D. Henry, H. Ben Hadid, and F. Rousset, “Stability of a flow down an incline with respect to two-dimensional and three-dimensional disturbances for Newtonian and non-Newtonian fluids,” *Phys. Rev. E* **92**, 063010 (2015).
- <sup>35</sup>P. J. Schmid, “Nonmodal stability theory,” *Annu. Rev. Fluid Mech.* **39**, 129 (2007).